Islamic Azad University

Journal of

Optoelectronical Nanostructures

Volume 10, Issue 2, Summer 2025, Page 84-105

Research Paper

High sensitivity surface plasmon resonance sensor based on D-shaped photonic crystal fiber using Ag/α-Fe_2O_3

Seyed Hossein Moayed, Mojtaba Sadeghi*, Zahra adelpour

Department of Electrical Engineering, Shi.C., Islamic Azad University, Shiraz, Iran

Received: **2024.11.19**
Revised: **2025.04.11**
Accepted: **2025.05.04**
Published: **2025.08.25**

Use your device to scan and read the article online

Keywords:
Photonic crystal fiber, Plasmonic, Nano sensor, Surface plasmon polariton

Abstract:
In the present study, an ultrahigh-sensitivity photonic crystal fiber (PCF) sensor which works based on the surface plasmon resonance (SPR) phenomenon is proposed. The structure is cut into a D-shape and two layers of Ag and hematite ($\alpha - Fe_2O_3$) materials are placed on the cut part. The $\alpha - Fe_2O_3$ layer prevents silver oxidation as well as significantly increases the interaction between light and the analyte, thereby increasing the efficiency of the sensor. In this structure, evanescent waves interact with the free electrons of the metal, and surface plasmon waves arise, based on which sensing is performed. The method of finite element (FEM) modeling is employed to investigate the response of the SPR sensor to the refractive index (RI). By examining the loss peak shift, the desired refractive indices can be identified. The presented PCF sensor provides a very high sensitivity of 9200 nm/RIU and also covers a detectable refractive index range of 1.3 to 1.4. The performance of the PCF-SPR sensor implies that it can be very suitable for use in applications such as biosensing and chemical detection.

Citation: Seyed Hossein Moayed, Mojtaba Sadeghi, Zahra Adelpour. High sensitivity surface plasmon resonance sensor based on D-shaped photonic crystal fiber using Ag/α-Fe2O3. **Journal of Optoelectronical Nanostructures.** 2025; 10 (2): 84-105.

***Corresponding author:** Mojtaba Sadeghi
Address: Department of Electrical Engineering, Shi.C., Islamic Azad University, Shiraz, Iran
Email: mojtaba.sadeghi@iau.ac.ir
DOI: https://doi.org/ 10.71577/jopn.2025.1191043

1. INTRODUCTION

Today, one of the most interesting topics in the field of sensing is SPR-based sensors. They have extraordinary capabilities in various applications such as interactions of antibody-antigen, biochemical/biological detection, and medical diagnostics [1-6]. SPR sensors leverage the unique properties of surface plasmons, which are the free electrons that oscillate collectively at the interface of metal-dielectric medium. These oscillations respond quickly to changes in the refractive index of the surrounding environment, which makes the SPR sensors excellent for real-time detection of molecular interactions. The three most commonly used types of SPR sensors are based on prism, fiber grating, and PCF. Prism based ones are large and less accurate than others. Fiber grating based sensors have moderate efficiency and their loss curves are almost wide, which makes it difficult to identify some analytes. In 1993, Jorgenson introduced an SPR-based optical fiber sensor, which successfully addressed the limitations of earlier designs [7]. PCFs, a type of microstructured optical fibers, are described by a periodic structure of air holes along the fiber axis. The compact physical dimensions of PCFs enable significant miniaturization of sensors. Furthermore, the guided modes in PCFs can be precisely controlled by tuning structural parameters and selecting appropriate materials, leading to enhanced sensing performance. Unlike traditional SPR sensors, PCF sensors offer several advantages, including smaller size, higher accuracy, and easier manufacturability. These sensors demonstrate exceptional performance characteristics including minimal loss, enhanced detection capability, rapid temporal response, non-label-dependent operation, continuous observation capacity, adaptable configuration, and consistent operational stability. These advantages of PCFs have driven significant interest in PCF-based SPR sensors, prompting researchers to develop novel configurations to further improve their performance characteristics. Consequently, PCF-SPR sensors have found widespread implementation across diverse detection domains, particularly in biomolecular interaction analysis and chemical compound monitoring [8,9].

Au and Ag are the most widely used as plasmonic materials. Au is chemically stabe and resistant to oxidation in adverse environments. However, the silver coating makes the sensor more sensitive and accurate. This is because the ratio of the real part to the imaginary part of the permittivity of silver is higher than that of gold. Also, silver has a higher reflection and absorption constant. Studies by Brujinet et al. proved silver achieves higher refractive index sensitivity than alternative SPR metals [10]. In 2019, Yasli et al. introduced a PCF SPR-based dual-channel sensor using gold and silver coatings. The gold-coated channel had a sensitivity of 2500 nm/RIU, and the silver-coated channel had a sensitivity of

3083 nm/RIU [11]. Another class of PCF-based sensors is the D-shaped, which brings the analyte closer to the core and increases the sensitivity. In 2022, Fanglong Meng et al. introduced a PCF-SPR refractive index sensor with a D-shaped structure that used a thin layer of gold. The sensitivity of this sensor is reported to be 5100 nm/RIU [12]. Vishal Sorathiya et al. in 2022, introduced the D-polished PCF sensor in which three layers of silver, graphene, and titanium dioxide (TiO2) were used. The sensitivity of this sensor is 4250 nm/RIU [13]. Fengmin Wang et al. in 2023, introduced a PCF-SPR sensor structure in which the analyte was internally injected into one of the cavities. The wavelength sensitivity of this structure was 9217.22 nm/RIU [14]. In 2024, J. Divya et al. designed a dual-channel D-shaped PCF-SPR sensor in which a gold layer was used for each channel. The sensitivity of the channels is reported as 6000 nm/RIU and 10000 nm/RIU. This sensor has a complex structure [15]. Ram Pravesh et al. in 2024, designed a double D-shaped dual-core biosensor that was cut on both sides to detect biomolecules in human blood. The sensitivity of this sensor is reported as 7500 nm/RIU [16].

To prevent silver oxidation and increase sensitivity, a layer of a suitable material can be placed on it. One of these materials that has recently received attention is Hematite ($\alpha - Fe_2O_3$), which is a type of iron oxide. Adding this substance increases the effective absorbance constant and thus the sensitivity of the sensor improves. It is a semiconductor material known for its good thermodynamic stability at high temperatures, non-toxicity, low cost, abundance and affordability. It is suitable for biomolecules in different environments [17]. In 2020, Kadhim et al. introduced an optical fiber D-shaped SPR sensor in which silver and $\alpha - Fe_2O_3$, were used as a grating. Their structure recognized refractive indices 1.33 and 1.39. The maximum sensitivity of 6400 nm/RIU had been calculated [18]. In 2022, Farhan Mumtaz et al. introduced a D-shaped fiber sensor with an Ag/$\alpha - Fe_2O_3$ layer. Their structure could detect refractive indices between 1.33 and 1.4, and by adding Fiber Bragg Grating (FBG) to the structure, it could also detect temperature changes. The sensitivity of this sensor was 8518 nm/RIU [17]. In 2023, Zhang et al. introduced an optical fiber SPR sensor in which a layer of gold was used together with $\alpha - Fe_2O_3$. This sensor successfully detected analytes with refractive indices ranging from 1.33 to 1.38 and its sensitivity was reported as 4800 nm/RIU [19].

In this research, we propose a highly sensitive surface plasmon resonance biosensor utilizing a D-shaped PCF platform with Ag/$\alpha - Fe_2O_3$ layer. Finite

element modeling was employed to characterize the optical performance of the sensor design. Numerical analysis reveals the sensor achieves very good performance metrics, including 9200 nm/RIU sensitivity and 1.1×10^{-5} RIU resolution. The optimized design maintains structural simplicity while covering the 1.33-1.41 refractive index range.

2. DESIGN AND THEORY

Figure 1(a) presents the cross-sectional layout of the proposed PCF-SPR sensor. Our structure is D-shaped and we have used air holes with a diameter of d_1, which are placed in a hexagonal arrangement. Also, a small air cavity with a diameter of d_2 is placed between the two lower air cavities. The pitch of holes is equal to Λ. In the upper part of the structure, we have used two thin layers of silver and $\alpha - Fe_2O_3$. The geometrical parameters and their sizes are given in Table 1. For accurate calculations, a perfect match layer (PML) is positioned around the computation zone's perimeter to capture emitted radiation. Furthermore, Fig. 1(b) displays the practical setup of the apparatus. A single-mode fiber connects the various elements, and the sensor is enclosed in a chamber with the analyte. Two ports—one for inlet and one for outlet—are managed by a single pump. Light from a broadband source is directed into the sensor after passing through a polarization controller, and the transmitted light is evaluated by an optical spectrum analyzer (OSA).

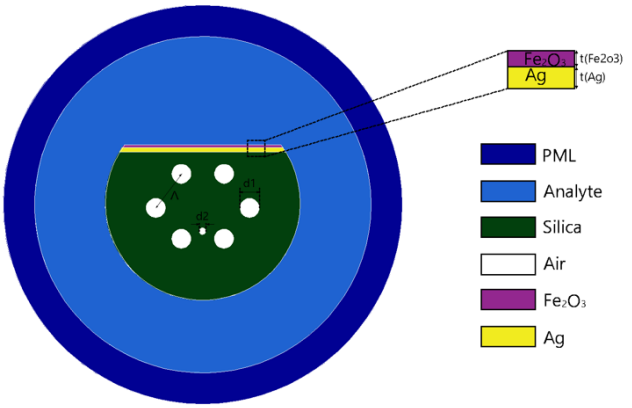

(a)

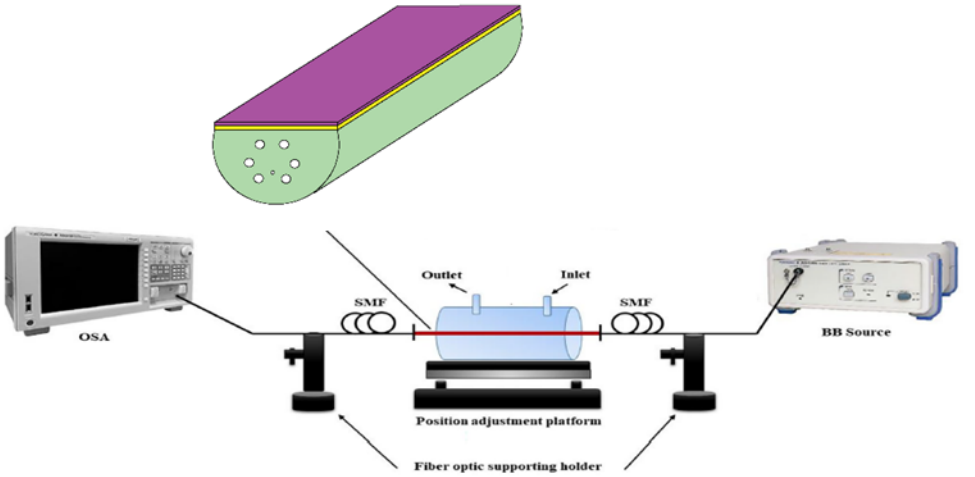

(b)

Fig. 1. (a) Cross-section of the proposed sensor, (b) the schematic of the laboratory setup of the proposed sensor

Table 1.
Geometrical parameters of the proposed sensor (Fig. 1)

Symbol	Parameter	Quantity (μm)
d1	Diameter of large rods	1.4
d2	Small rod diameter	0.7
d3	Fiber diameter (internal)	10
Λ	Pitch	3.5
t_{Ag}	Thickness of the silver layer	0.05
$t(Fe_2O_3)$	Thickness of $\alpha - Fe_2O_3$ layer	0.015

The background material of the sensor is silica, whose dispersion relation is determined by the Sellmeier equation as follows [20]:

$$n^2 - 1 = \frac{A_1\lambda^2}{\lambda^2 - B_1^2} + \frac{A_2\lambda^2}{\lambda^2 - B_2^2} + \frac{A_3\lambda^2}{\lambda^2 - B_3^2} \quad (1)$$

In this formula, n stands for the refractive index of the material, while λ represents the wavelength of the incoming light. The constants A_1, A_2, A_3, B_1, B_2,

and B_3 are set at 0.6961663, 0.4079426, 0.8974790, 0.0684043, 0.1162414, and 9.8961610, respectively. The silver layer's dispersion is described by the Drude model [16]:

$$\varepsilon_m(\lambda) = 1 - \frac{\lambda^2 \lambda_c}{\lambda_P^2(\lambda_c + i\lambda)} \quad (2)$$

With λ_c as the collision wavelength associated with energy losses and λ_P as the plasma wavelength. For silver, these values are $\lambda_c = 17.614$ μm and $\lambda_P = 0.14541$ μm. The refractive index of $\alpha - Fe_2O_3$ has been assessed through various practical investigations, grounded in theoretical equations provided in references [18, 19, 21, 22, 23]:

Type equation here.

$$n_{\alpha-Fe_2O_3} = \frac{1+R}{1-R} + \sqrt{\frac{4R}{(1+R)^2} - k^2} \quad (3)$$

In the above relationship, R is the reflection coefficient and is equal to:

$$R = 1 - \sqrt{T \times \exp(A)} \quad (4)$$

where T represents the transfer function and A represents the absorption rate of $\alpha - Fe_2O_3$ layer. Also, k is the extinction constant and its relationship with the absorption constant α is equal to:

$$k = \frac{\alpha\lambda}{4\pi} \quad (5)$$

$$\alpha = \frac{1}{t} \ln \frac{1}{T} \quad (6)$$

Where t is the thickness of $\alpha - Fe_2O_3$ layer. In our proposed structure, silver is used to stimulate the SPR. When SPR occurs, coupling between core mode and SPR mode can happen. This coupling between modes can be expressed using coupling mode theory as follows [24]:

$$\begin{cases} \frac{E_1}{z} = i\beta_1 E_1 + i\kappa E_2 \\ \frac{E_2}{z} = i\beta_2 E_2 + i\kappa E_1 \end{cases} \quad (7)$$

where E_1 and E_2 are the electric field corresponding to core and SPP modes, β_1 and β_2 are their propagation constants, κ represents the coupling strength and z is the propagation length. In the coupling mode, which is also called resonance

mode, the phase matching conditions are provided, and this will be when β_1 and β_2 are equal. In fact, in the resonant mode, the maximum energy is transferred from the core to the SPP mode.

Confinement loss serves as a critical metric for assessing PCF-SPR sensor performance, quantifiable through the following analytical expression [25]:

$$Loss(^{dB}/_{cm}) = 8.86 \times \frac{2\pi}{\lambda} Im(n_{eff}) \times 10^4 \quad (8)$$

Here, $Im(n_{eff})$ denotes the imaginary component of the effective refractive index. The wavelength sensitivity, another critical performance metric for PCF-SPR sensors, is determined by [26]:

$$S_\lambda(nm/RIU) = \partial\lambda_{peak}/\partial n_a \quad (9)$$

Where $\partial\lambda_{peak}$ is the resonance frequency shift and ∂n_a is the refractive index changes related to the resonance frequencies. Sensor resolution, an additional critical metric for performance evaluation, is derived from the subsequent expression. [27]:

$$R = \Delta n_a \frac{\Delta\lambda_{min}}{\Delta\lambda_{peak}} \quad (10)$$

Here, Δn_a corresponds to the analyte's refractive index variation, $\Delta\lambda_{peak}$ is the shift in resonance wavelength and $\Delta\lambda_{min}$ denotes the sensor's minimum detectable wavelength shift. The value of $\Delta\lambda_{min}$ is usually set to 0.1 in OSA. There is another important parameter called FOM which is considered for better detection limits. FOM is obtained from the following formula [28]:

$$FOM = \frac{S_\lambda}{\text{FWHM}} \quad (11)$$

Where S_λ the wavelength sensitivity obtained from Eq. (9) and FWHM is represents the spectral bandwidth measured at half-maximum intensity.

3. RESULTS AND DISCUSSIONS

For the simulation, we utilize the Finite Element Method (FEM) facilitated by COMSOL Multiphysics, a commercial software tool. Resonance between the core mode and the surface plasmon polariton (SPP) mode occurs when their phase-matching condition is satisfied, meaning the wave vector of the core mode's incident light matches that of the SPP mode's surface plasmon waves, resulting in the peak transfer of energy from the core mode to the SPP mode. The

distribution of the optical field related to the core (fundamental) modes, SPP and resonant mode are illustrated in Fig. 2(a), (b), (c), respectively. The results have been obtained based on an analyte RI of 1.41 and y-polarized (vertical direction). The field distribution is related to the core and SPP modes at a wavelength of 1 μm, with the resonant mode appearing at 1.032 μm.

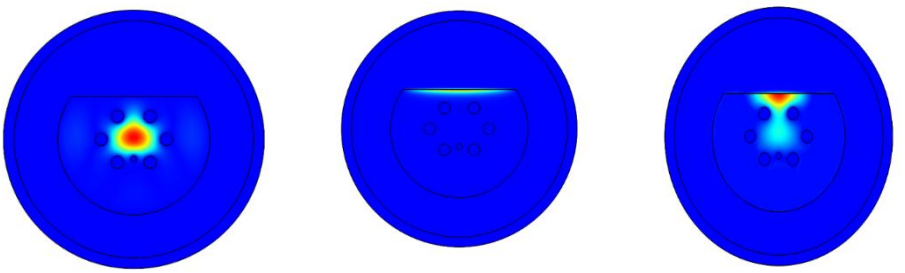

(a) **(b)** **(c)**

Fig. 2. Distribution of the y-polarized optical field with n=1.41 (a) Field distribution of the core mode (fundamental mode) at a wavelength of 1 μm (b) Distribution of the field in SPP mode at a wavelength of 1 μm (c) Distribution of the field in resonance mode at a wavelength of 1.032 μm

Fig. 3 illustrates the loss spectrum and the dispersion interplay between the fundamental mode and the surface plasmon mode at $n = 1.41$. The real components of the effective refractive indices for both the core mode and SPP mode, as well as the confinement loss (representing the imaginary component of the effective refractive index), are drawn in terms of different wavelengths. As can be seen, the confinement loss increases with increasing wavelength until it reaches the maximum (55.3 $^{dB}/_{cm}$ at 1.032 μm) and then decreases again. Meanwhile, the real parts of the effective refractive indices for the core and SPP modes decline with rising wavelength, and when they become equal, the resonance conditions are met and the loss peak occurs.

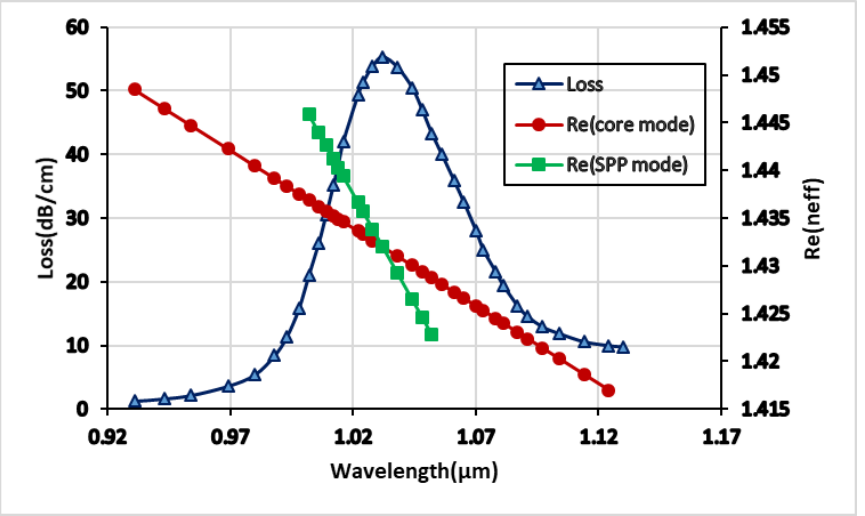

Fig. 3. Dispersion relation for core mode and SPP mode. The refractive index of the analyte in this case is considered to be 1.41. The maximum loss in resonant mode is equal to 55.3 dB/cm and occurred at a wavelength of 1.032 μm

Next, we examine the effect of changing the geometric parameters of the proposed structure. Fig. 4 displays the variation of the loss spectrum with different diameters of air holes (d_1) assuming n=1.41. As d_1 rises from 1.3 to 1.5 μm, confinement loss decreases and the resonance wavelength moves to higher wavelengths (redshift). This decrease in loss stems from the reduced modal area of the core as air hole size grows, limiting energy transfer from the core mode to the SP mode due to a constricted pathway between the core and the plasmonic surface, thereby lowering the overall loss.

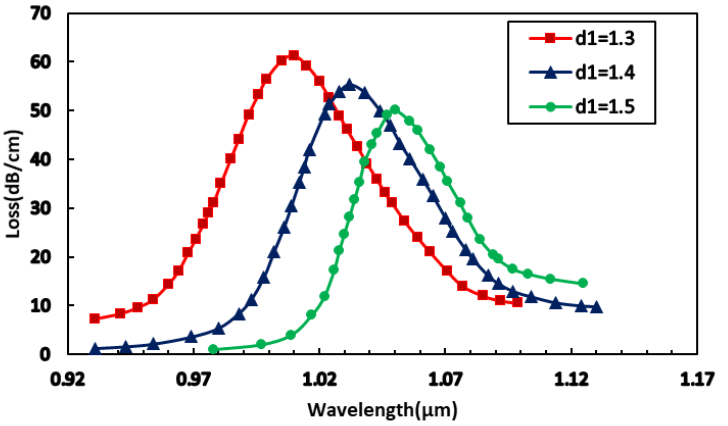

Fig. 4. Confinement loss diagram for variations in the diameter of large air holes (d_1). The refractive index of the analyte is considered to be 1.41. Other parameters are similar to the Table 1

Fig. 5 illustrates the effect of changing the value of Λ on the confinement losses. As it is clear, with the variation of Λ from 3.3 μm to 3.6 μm (by keeping other parameters constant and d_1=1.4 μm), the resonance wavelength changes from 1.13 μm to 0.98 μm. Also, the maximum confinement loss value increases from 48.6 $^{dB}/_{cm}$ to 55.3 $^{dB}/_{cm}$ and then decreases to 51.5 dB/cm.

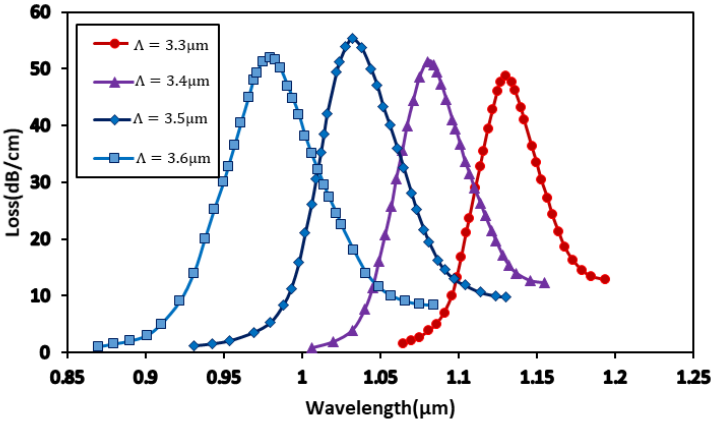

Fig. 5. Confinement loss diagram for pitch variations (Λ), (RI=1.41, d_1=1.4μm)

As Λ increases, the core energy finds a wider path to reach the SP mode in front of it, and as a result, more energy reaches the plasmonic surface and losses increase. However, as Λ increases further, some of the core energy is scattered in the structure and wasted as leakage, and as a result, losses decrease. Also, with Λ changes, the phase-matching conditions change, which leads to a shifting the resonance wavelength. According to the obtained results, the optimal values for d_1 and Λ are considered as 1.4 and 3.5 μm, respectively.

In the next step, we examine the effect of changing the thickness of Ag and $\alpha - Fe_2O_3$ layers. The Ag layer thickness is adjusted from 45 to 60 nm, with d_1 = 1.4 μm, Λ = 3.5 μm, an analyte refractive index of 1.41, and $\alpha - Fe_2O_3$ thickness fixed at 15 nm. Results are presented in Fig. 6. At an Ag thickness of 45 nm, the peak loss reaches 57.5 $^{dB}/_{cm}$ with resonance at 0.98 μm. For 50 nm, 55 nm, and 60 nm thicknesses, peak losses are 55.3 $^{dB}/_{cm}$ at 1.032 μm, 37.6 $^{dB}/_{cm}$ at 1.086 μm, and 26.1 $^{dB}/_{cm}$ at 1.145 μm, respectively. This occurs because thicker silver layers modify the real part of the $Re(n_{ff})$ of the SPP, causing a wavelength shift. Additionally, a thicker silver layer weakens the evanescent field before it reaches the interface of the metal-analyte, requiring polaritons to travel farther, reducing their energy for interaction with the analyte and thus lowering confinement loss. Variations in silver thickness also alter the $Re(n_{ff})$ of the plasmonic material and structure, adjusting phase-matching conditions and shifting the resonance wavelength.

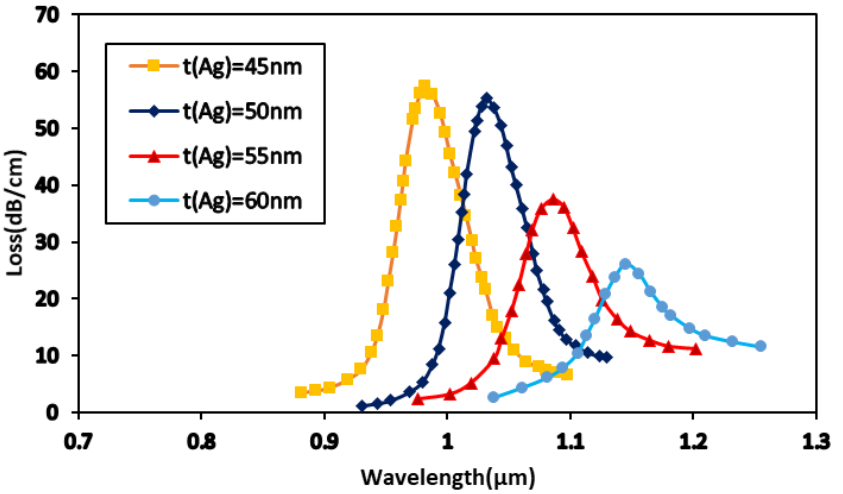

Fig. 6. Variations of confinement loss with different silver layer thickness. (RI=1.41, d_1=1.4μm, $t(\alpha - Fe_2O_3) = 15nm$)

Figure 7 illustrates how the loss spectrum changes with different $\alpha - Fe_2O_3$ layer thicknesses, with d_1 = 1.4 μm, Λ = 3.5 μm, an analyte RI of 1.41, and Ag thickness at 50 nm. As α-Fe_2O_3 thickness increases, confinement loss rises slightly, the resonance wavelength shifts to longer values, and the FWHM of the loss spectrum broadens.

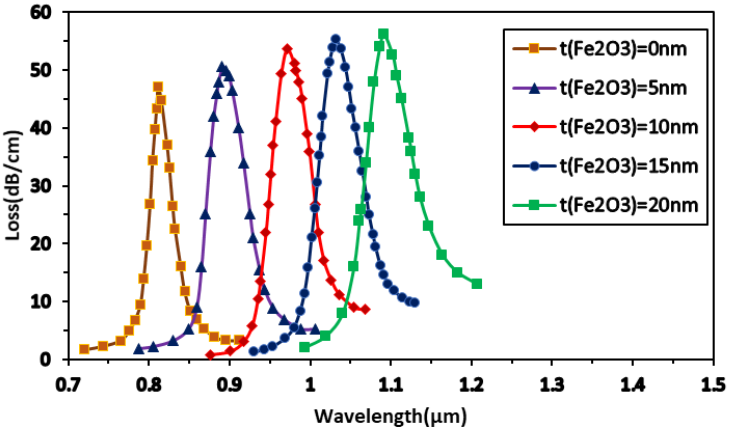

Fig. 7. Variations of confinement loss with different $\alpha - Fe_2O_3$ layer thickness. (RI=1.41, d1=1.4μm, t(Ag)=50nm)

Figure 7 can be explained as follows: to form an evanescent field, the thickness of the $\alpha - Fe_2O_3$ layer must be proportional to the penetration depth, a small thickness of the $\alpha - Fe_2O_3$ layer causes the evanescent field to not form well, and as a result, less energy reaches the $\alpha - Fe_2O_3$ -analyte interface and a weaker interaction occurs between the analyte and the light energy, and losses are reduced. As the $\alpha - Fe_2O_3$ thickness increases, the evanescent field becomes stronger and the interaction also improves, and as a result, losses increase. As we can see in Fig. 7, as $\alpha - Fe_2O_3$ thickness grows from 0 to 20 nm, the loss peak values change from 47 $^{dB}/_{cm}$ to 56.1 $^{dB}/_{cm}$, and the resonance wavelength shift towards the longer wavelengths. To choose the appropriate thickness for the silver and $\alpha - Fe_2O_3$ layers, we also investigate the maximum sensitivity, FWHM, and FOM parameters. Figure 8 shows resonance wavelength changes for various analyte RIs as Ag and α-Fe_2O_3 layer thicknesses are changed. Also, Table 2 summarizes the sensitivity values obtained for varying thicknesses of the Ag and $\alpha - Fe_2O_3$ layers.

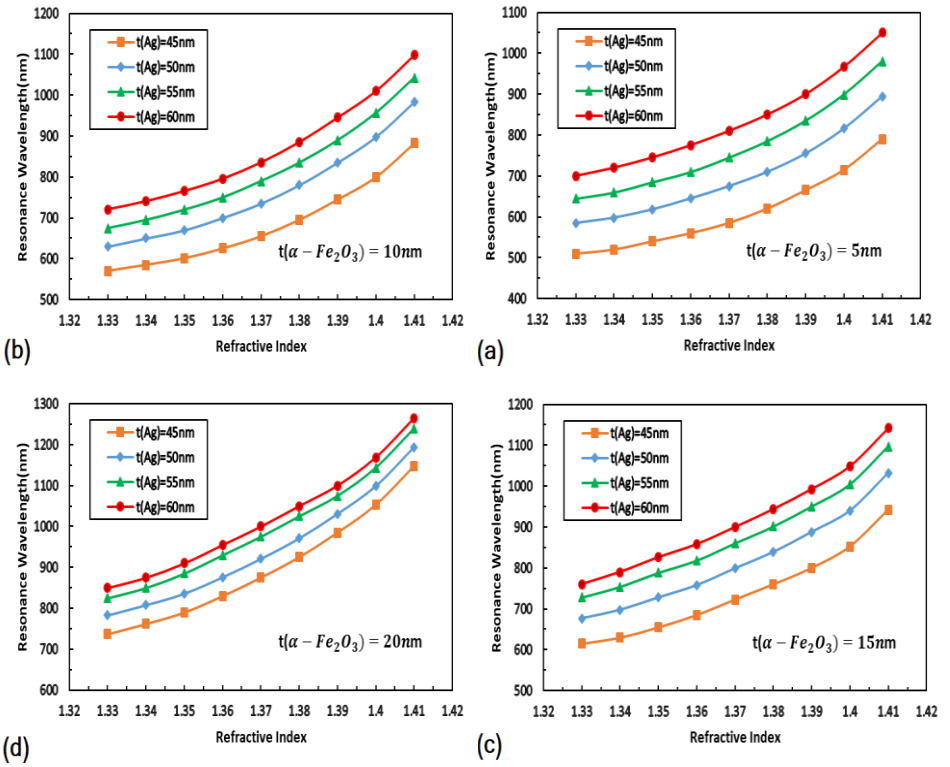

Fig. 8. Diagram of resonant wavelengths in different refractive indices of the analyte for different values of silver layer thickness (a) in the case of $\alpha - Fe_2O_3$=5nm, (b) in the case of $\alpha - Fe_2O_3$ =10nm, (c) in the case of $\alpha - Fe_2O_3$=15nm and (d) in the case of $\alpha - Fe_2O_3$ =20nm

From Table 2, it's evident that sensitivity is enhanced with a thicker Ag layer as well as increasing the thickness of $\alpha - Fe_2O_3$. According to Fig. 6 and Table 2, we opt for an Ag thickness of 50 nm. On the other hand, according to Fig. 7, with the increase in the thickness of the $\alpha - Fe_2O_3$ layer, the FWHM increases, which can cause a decrease in FOM as a result of a decrease in the efficiency of the sensor. Sensitivity and FOM values for different thicknesses of the $\alpha - Fe_2O_3$ layer are drawn in Fig. 9. By increasing the thickness of $\alpha - Fe_2O_3$ to 15 nm, the value of FOM reaches the maximum value of 150.82 RIU^{-1}, and after that, for a thickness of 20 nm of $\alpha - Fe_2O_3$ the amount FOM drops sharply and reaches 127 RIU^{-1}. At the maximum of FOM, sensitivity is 9200 nm/RIU. According to the calculated results, the thickness of $\alpha - Fe_2O_3$ layer equal to 15 nm is chosen as the optimal value.

Table 2.
Sensor sensitivity values for different thicknesses of silver layer and $\alpha - Fe_2O_3$

	$(^{nm}/_{RIU})S$			
	t(Ag) = 45nm	***t(Ag) = 50nm***	***t(Ag) = 55nm***	***t(Ag) = 60nm***
$t(\alpha - Fe_2O_3) = 5nm$	7500	7900	8100	8320
$t(\alpha - Fe_2O_3) = 10nm$	8300	8550	8600	8800
$t(\alpha - Fe_2O_3) = 15nm$	8950	9200	9300	9400
$t(\alpha - Fe_2O_3) = 20nm$	9460	9520	9580	9600

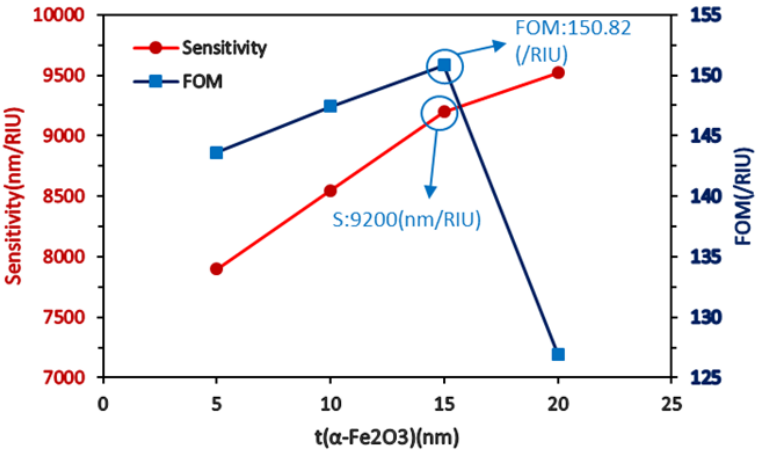

Fig. 9. Diagram of sensor sensitivity and FOM values for different values of $\alpha - Fe_2O_3$ layer thickness. The thickness of the gold layer is 50 nm and the refractive index of the analyte is 1.41.

Also, Fig. 10 shows the changes in resonance wavelength for different refractive indices of the analyte. It can be seen that the sensor shows a very good performance in terms of linearity in refractive indices of 1.34 to 1.4.

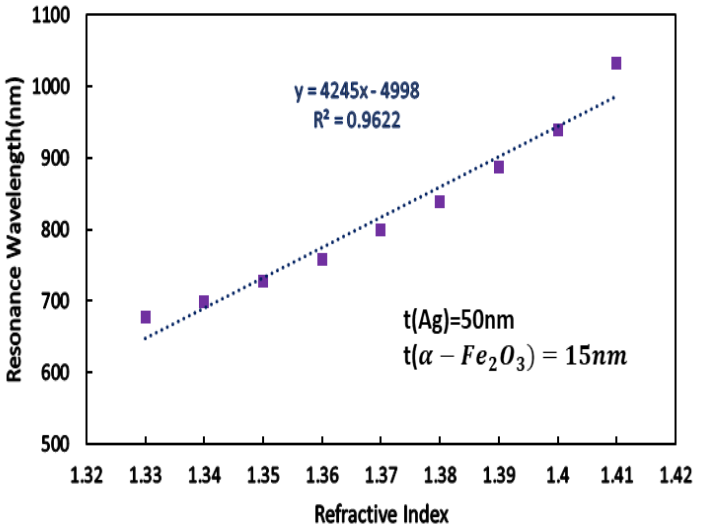

Fig. 10. Variation of the resonance wavelength with refractive indices of analytes

Fig. 11 depicts confinement loss spectra for analytes of diverse RIs.

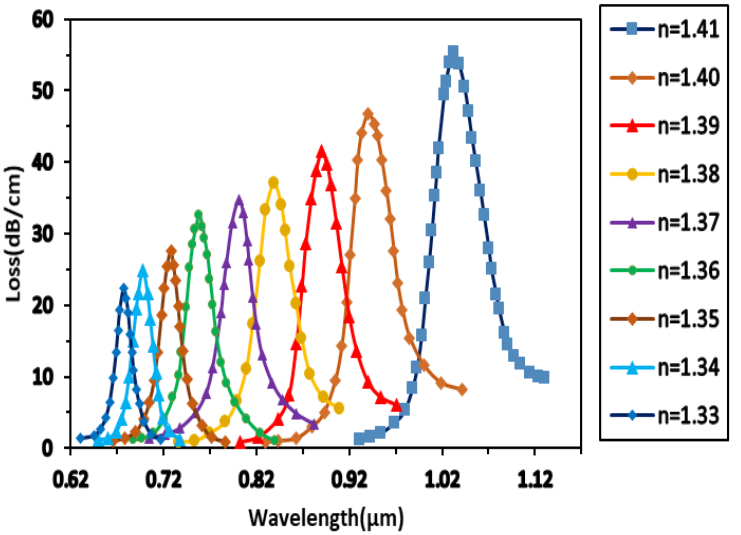

Fig. 11. Confinement loss peak and resonance wavelength with different analyte RIs. The geometric parameters of the structure are as shown in Table 1

Also, efficiency parameters for the proposed sensor for different values of analyte RIs are given in Table 3, indicating a sensitivity of 9200 nm/RIU and a resolution of $1.1 \times 10^{-5} RIU$, suggesting this structure is well-suited for refractive index diagnostic purposes.

Table 3.
The efficiency parameters of the proposed sensor for different refractive index of the analyte

RI	Resonance wavelength (nm)	Loss (dB/cm)	Sensitivity (nm/RIU)	Resolution (RIU)	FWHM (nm)	FOM (RIU^{-1})
1.33	677	22.4	-	-	21	-
1.34	698	24.9	2100	4.76×10^{-5}	24	87.5
1.35	728	27.6	3000	3.3×10^{-5}	31	96.7
1.36	760	32.6	3200	3.1×10^{-5}	33	97
1.37	800	34.7	4000	2.5×10^{-5}	40	100
1.38	843	37	4300	2.3×10^{-5}	43	100
1.39	890	41.5	4700	2.1×10^{-5}	46	102
1.40	940	46.7	5000	2×10^{-5}	49	103
1.41	1032	55.3	9200	1.1×10^{-5}	61	150.8

Table 4 compares the performance of the proposed sensor with previously reported SPR designs.

Table 4.
Comparison of the proposed sensor with some researches

Year/Ref.	Sensor structure	RI Range	S_λ[nm /RIU]	Resolution [RIU]
2018[29]	D-type PCF based plasmonic (gold)	1.36-1.38	3340	5.98×10^{-6}
2020[18]	D-Shaped optical fiber SPR sensor grating($\alpha - Fe_2O_3$)	1.33-1.39	6400	1.56×10^{-6}
2021/[30]	D-type PCF based plasmonic (silver)	1.36-1.41	7400	1.35×10^{-6}
2022[12]	D-type PCF based plasmonic (gold)	1.35-1.40	5100	-
2022[17]	Optical fiber SPR sensor($\alpha - Fe_2O_3$)	1.33-1.4	8518	-
2023[31]	D-type optical fiber based plasmonic (silver-graphene oxide)	1.30-1.34	833.3	-
2023[16]	PCF based plasmonic	1.41-1.58	9217	1.08×10^{-6}
2023/[19]	Optical fiber SPR sensor($\alpha - Fe_2O_3$)	1.33-1.38	4800	-
2024[15]	Dual core D-Shaped PCF sensor	1.33-1.40	7500	-
Our research	Optical fiber SPR sensor($\alpha - Fe_2O_3$)	1.33-1.41	9200	1.10×10^{-6}

4. CONCLUSION

This study presents and numerically assesses a D-shaped PCF-SPR sensor with elevated sensitivity sensor coated by Ag and hematite ($\alpha - Fe_2O_3$) layers. The sensor was designed to operate within a RI range of 1.33 to 1.41, making it suitable for a wide variety of biosensing and chemical detection applications. The use of a thin $\alpha - Fe_2O_3$ layer not only enhanced the sensor's sensitivity but also

provided protection against silver oxidation, ensuring long-term stability and performance. Through rigorous FEM simulations, we optimized critical structural aspects, including air hole sizes, pitch, and the thicknesses of the Ag and $\alpha - Fe_2O_3$ coatings. The sensor achieves a striking wavelength sensitivity of 9200 nm/RIU and a resolution of 1.1×10^{-5} RIU, which are among the highest reported values for PCF-based SPR sensors. The sensor's performance was further validated by its excellent linearity across the tested RI range and its ability to achieve a high FOM of 150.82 RIU^{-1}. The key advantages of this sensor include its simple design, ease of fabrication, and superior sensitivity, making it a viable option for real-world applications in medical diagnostics, environmental monitoring, and chemical sensing. The integration of $\alpha - Fe_2O_3$ as a protective and enhancing layer opens new avenues for improving the durability and performance of SPR-based sensors. Future work could focus on experimental validation of the proposed design and further optimization for specific applications, such as the detection of biomolecules or gases. Additionally, the sensor's performance could be enhanced by exploring alternative materials or nanostructures for the plasmonic layers. Overall, this study contributes to the growing field of optical sensing by providing a robust and highly sensitive platform for refractive index detection.

Declaration of Competing Interest

The authors declare that they have no known competing financial interests or personal relationships that could have appeared to influence the work reported in this paper.

REFERENCES

[1] Mansuri, M., Mir, A., & Farmani, A. (2019) Numerical modeling of a nanostructure gas sensor based on plasmonic effect. Journal of Optoelectronical Nanostructures 4(2): 29-44. https://dorl.net/dor/20.1001.1.24237361.2019.4.2.3.3

[2] Vasimalla, Y., Salah, N. H., Santhosh, C., Balaji, R., Rasul, H. M., Srither, S. R., & Kumar, S. (2025) SMF-based SPR sensors utilizing thallium bromide immobilization for detection of various bacterial cells. Microchemical Journal 208:112312. https://doi.org/10.1016/j.microc.2024.112312

[3] Nasrolahi, M., Farmani, A., Horri, A., & Hatami, H. (2024) FDTD Analysis of a High-sensitivity refractive index sensing based on Fano resonances in a

plasmonic planar split-ring resonators. Journal of Optoelectronical Nanostructures 9(3):1-12. DOI: 10.30495/JOPN.2024.33499.1321

[4] Pirhaghshenasvali, S., Ghayour, R., & Vaghefi, M. (2024) High-Performance Biosensor by using Au Nanoparticles and Grating for Sensing Waterborne Bacteria in Drinking Water. Journal of Optoelectronical Nanostructures, 9(1):16-36. https://doi.org/10.30495/jopn.2024.32587.1303

[5] Karimi, A., Jabbari, M., & Solookinejad, G. (2023) Design and simulation of metal-insulator-metal waveguide for filtering and sensor applications. Journal of Optoelectronical Nanostructures, 8(3): 90-109. https://doi.org/10.30495/jopn.2023.31705.1284

[6] M. Olyaee, M. B. Tavakoli & A. Mokhtari (2019) Propose, Analysis and Simulation of an All Optical Full Adder Based on Plasmonic Waves using Metal-Insulator-Metal Waveguide Structure. Journal of Optoelectronical Nanostructures. 54 (9):6227. https://journals.marvdasht.iau.ir/article_3622_345ca515d72d1b069f68df919aba7b29.pdf

[7] Jorgenson, R. C., & Yee, S. S. (1993) A fiber-optic chemical sensor based on surface plasmon resonance. Sensors and Actuators B: Chemical 12(3): 213-220. https://doi.org/10.1016/0925-4005(93)80021-3

[8] Zhang, Q., Cheng, C. E., Huang, C., Liao, X., Wang, Y., Tang, J., ... & Liu, J. (2025) Highly Sensitive PCF Sensor Based on Au-TiO 2 for Cancer Cell Detection. IEEE Sensors Journal 25(6):9664-9674. https://doi.org/10.1109/JSEN.2025.3537767

[9] Mahmud, R. R., Anzum, M. S., Hassan, A. A., Rafsan, A. A., Salimullah, S. M., & Nayan, M. F. (2025) Dual-side polished SPR-PCF ultra-wide refractive index sensor with high amplitude sensitivity. Journal of Optics 27(2): 025101. DOI :10.1088/2040-8986/ada4bd

[10] de Bruijn, H. E., Kooyman, R. P., & Greve, J. (1992) Choice of metal and wavelength for surface-plasmon resonance sensors: some

considerations. Applied optics 31(4):440_1-442. https://doi.org/10.1364/AO.31.0440_1

[11] Yasli, A., Ademgil, H., Haxha, S., & Aggoun, A. (2019) Multi-channel photonic crystal fiber based surface plasmon resonance sensor for multi-analyte sensing. IEEE Photonics Journal 12(1): 1-15. https://doi.org/10.1109/JPHOT.2019.2961110

[12] Meng, F., Wang, H., & Fang, D. (2022) Research on D-shape open-loop PCF temperature refractive index sensor based on SPR effect. IEEE Photonics Journal 14(3):1-5. https://doi.org/10.1109/JPHOT.2022.3166822

[13] Sorathiya, V., Lavadiya, S., Faragallah, O. S., Eid, M. M., & Rashed, A. N. Z. (2022) D shaped dual core photonics crystal based refractive index sensor using graphene–titanium–silver materials for infrared frequency spectrum. Optical and Quantum Electronics 54(5):290. https://doi.org/10.1007/s11082-022-03700-0

[14] Wang, F., Wei, Y., & Han, Y. (2023) High sensitivity and wide range refractive index sensor based on surface plasmon resonance photonic crystal fiber. Sensors 23(14):6617. https://doi.org/10.3390/s23146617

[15] Divya, J., Selvendran, S., Raja, A. S., & Borra, V. (2023) A novel plasmonic sensor based on dual-channel D-shaped photonic crystal fiber for enhanced sensitivity in simultaneous detection of different analytes. IEEE Transactions on Nanobioscience 23(1):127-139. https://doi.org/10.1109/TNB.2023.3294330

[16] Pravesh, R., Kumar, D., Pandey, B. P., Chaudhary, V. S., & Kumar, S. (2024) Design and analysis of a double D-shaped dual core PCF sensor for detecting biomolecules in the human body. IEEE Sensors Journal 24(9):14159-14166. https://doi.org/10.1109/JSEN.2024.3380095

[17] Mumtaz, F., Roman, M., Zhang, B., Abbas, L. G., Ashraf, M. A., Fiaz, M. A., & Huang, J. (2022) A simple optical fiber SPR sensor with ultra-high sensitivity for dual-parameter measurement. IEEE Photonics Journal 14(5):1-7. https://doi.org/10.1109/JPHOT.2022.3203930

[18] RA. Kadhim, L. Yuan, H. Xu, J. Wu, Z. Wang. (2020) Highly sensitive D-shaped optical fiber surface plasmon resonance refractive index sensor based

on Ag-α-Fe2O3 grating. IEEE Sensors Journal. 20(17):9816-24. https://doi.org/10.1109/JSEN.2020.2992854

[19] Zhang, K. K., Wang, Y. Y., Wang, Q., Wang, H. Y., Qian, Y. Z., Zhang, D. Y., ... & Zhang, L. (2023) Sensitive monitoring of refractive index by surface plasmon resonance (SPR) with a gold α-iron (III) oxide thin film. Instrumentation Science & Technology 51(5):558-573. https://doi.org/10.1080/10739149.2023.2180030

[20] Mukhopadhyay, A. K., Sarkar, S., Mukherjee, S., & Das, N. R. (2024) Optimization and characterization of a PCF-based SPR sensor for enhanced sensitivity and reliability in diverse chemical and biological applications. Journal of the Optical Society of America B 42(1): 97-104. https://doi.org/10.1364/JOSAB.537519

[21] Kumar, P., Rawat, N., Hang, D. R., Lee, H. N., & Kumar, R. (2015) Controlling band gap and refractive index in dopant-free α-Fe_2O_3 films. Electronic Materials Letters 11:13-23. https://doi.org/10.1007/s13391-014-4002-0

[22] Elouafi, A., Moubah, R., Tizliouine, A., Derkaoui, S., Omari, L. H., & Lassri, H. (2020) Effects of Ru doping and of oxygen vacancies on the optical properties in α-Fe_2O_3 powders. Applied Physics A 126: 1-7. https://doi.org/10.1007/s00339-020-3385-z

[23] Al-Kuhaili, M. F., Saleem, M., & Durrani, S. M. A. (2012). Optical properties of iron oxide (α-Fe_2O_3) thin films deposited by the reactive evaporation of iron. Journal of alloys and compounds 521:178-182. https://doi.org/10.1016/j.jallcom.2012.01.115

[24] Wang, Y., Li, S., Li, J., Zhang, Z., Zhang, S., & Wu, J. (2019) High-sensitivity photonic crystal fiber refractive index sensor based on directional coupler. Optical Fiber Technology 49:16-21. https://doi.org/10.1016/j.yofte.2019.01.015

[25] Majeed, M. F., & Ahmad, A. K. (2024) Design and analysis of a high sensitivity open microchannel PCF-based surface plasmon resonance refractometric sensor. Optical Materials 147:114617. https://doi.org/10.1016/j.optmat.2023.114617

[26] Tuaimah, A. M., Tahhan, S. R., Taher, H. J., Ahmed, K., & Al-Zahrani, F. A. (2024) Multi analyte detection based on D-shaped PCF sensor for glucose

concentrations sensing. Optical and Quantum Electronics 56(3):319. https://doi.org/10.1007/s11082-023-05894-3

[27] Sardar, M. R., & Faisal, M. (2024) Dual-core dual-polished PCF-SPR sensor for cancer cell detection. IEEE Sensors Journal 24(7): 9843-9854. https://doi.org/10.1109/JSEN.2024.3358173

[28] Hassan, A. A., Nafiz, A. A. M., Mahmud, R. R., Nayan, M. F., & Salimullah, S. M. (2024) Investigation of dual plasmonic material integrated wrench-shaped PCF sensor with broadband resonance for cancer cell & chemical detection. Optik 318:172092. https://doi.org/10.1016/j.ijleo.2024.172092

[29] Lu, J., Li, Y., Han, Y., Liu, Y., & Gao, J. (2018) D-shaped photonic crystal fiber plasmonic refra ctive index sensor based on gold grating. Applied optics 57(19):5268-5272. https://doi.org/10.1364/AO.57.005268

[30] Liu, C., Shen, T., Liang, H., Chen, J. J., & Yang, T. (2021, September) Surface plasmon resonance refractive index sensor based on photonic crystal fiber with silver film and titanium dioxide film. In 2021 IEEE 6th Optoelectronics Global Conference (OGC) (pp. 47-51). IEEE. https://doi.org/10.1109/OGC52961.2021.9654350

[31] Amiri, I. S., Alwi, S. A. K., Raya, S. A., Zainuddin, N. A. A. M., Rohizat, N. S., Rajan, M. M., & Zakaria, R. (2023) Graphene oxide effect on improvement of silver surface plasmon resonance D-shaped optical fiber sensor. Journal of Optical Communications 44(1):53-60. https://doi.org/10.1016/j.rinp.2019.02.026